Available online at www.sciencedirect.com
ScienceDirect
Journal of Power Sources 173 (2007) 404–414
JOURNAL OF POWER SOURCES
www.elsevier.com/locate/jpowsour

Application of lattice Boltzmann method to a micro-scale flow simulation in the porous electrode of a PEM fuel cell

J. Park, M. Matsubara, X. Li *

Department of Mechanical and Mechatronics Engineering, University of Waterloo, 200 University Avenue W., Waterloo, Ontario, Canada N2L 3G1

Received 9 February 2007; received in revised form 1 April 2007; accepted 3 April 2007
Available online 18 April 2007

Abstract

The electrode of a PEM fuel cell is a porous medium generally made of carbon cloth or paper. Such a porous electrode has been widely modeled as a homogeneous porous medium with a constant permeability in the literature of PEM fuel cell. In fact, most of gas diffusion media are not homogeneous having non-isotropic permeability. In case of carbon cloth, the porous structure consists of carbon fiber tows, the bundles of carbon fiber, and void spaces among tows. The combinational effect of the void space and tow permeability results in the effective permeability of the porous electrode. In this work, the lattice Boltzmann method is applied to the simulation of the flow in the electrode of a PEM fuel cell. The electrode is modeled as void space and porous region which has certain permeability and the Stokes and Brinkman equations are solved in the flow field using the lattice Boltzmann model. The effective permeability of the porous medium is calculated and compared to an analytical calculation showing a good agreement. It has been shown that the permeability of porous medium is strongly dependant on the fiber tow orientation in three-dimensional simulations. The lattice Boltzmann method is an efficient and effective numerical scheme to analyze the flow in a complicated geometry such as the porous medium.

Keywords: LB; Lattice Boltzmann method; PEM fuel cell; Gas diffusion layer; Porous medium

1. Introduction

The demand for energy has been rising in all its forms while supplies of key fossil fuels have shown signs of decline during the last few decades. The consequent rising prices are likely to push us towards alternative energy sources. Fuel cells and hydrogen technology have been at the center of highly active research with viable early markets among the renewable energy alternatives. The polymer electrolyte membrane (PEM) fuel cell is now regarded as a promising alternative of internal combustion engine owing to its competitive power density with high efficiency as well as zero tailpipe emission [1].

A PEM cell consists of a membrane electrolyte assembly (MEA) sandwiched between two bipolar plates as shown in Fig. 1. The gas diffusion layer (GDL), catalyst layer and polymer electrolyte membrane are referred to as MEA where current is produced. Fuel and oxidant are supplied to both sides of MEA through the flow channels on the bipolar plates producing electron in the anode catalyst layer and water in the cathode catalyst layer. The GDL is a porous medium generally made of carbon cloth or paper and plays an essential role in fuel cells of permitting gas to be transported from the flow channel to the catalyst layer. The GDL must permit liquid water to be transported from the catalyst layer into the flow channels to remove the liquid water from the cell. When the liquid water is accumulated in the GDL the gas transport from the gas flow channel to the catalyst layer is hindered limiting the performance of a PEM fuel cell. Such water flooding is acute at the cathode side where the water is formed. The GDL also has to supply sufficient conductivity to shuttle the electrons between the catalyst layer and the bipolar plate. Normally, the conductivity of the GDL is inversely proportional to the thickness and porosity. Therefore, finding optimal values of the GDL parameters such as thickness, porosity, permeability and wetting characteristics have been important issues among PEM fuel cell researchers [2–6]. The pores can be hydrophobic with optimal value of polytetrafluoroethylene

* Corresponding author. Tel.: +1 519 888 4567x36843; fax: +1 519 885 5862.
E-mail address: x6li@uwaterloo.ca (X. Li).

0378-7753/$ – see front matter © 2007 Elsevier B.V. All rights reserved.
doi:10.1016/j.jpowsour.2007.04.021

Nomenclature

a	the distance from the center to the edge of the ellipse on the major axis
b	the distance from the center to the edge of the ellipse on the semi-major axis
c	$\delta x/\delta t$
c_s	sound speed
$\mathbf{e}_i$	velocity vector for the lattice Boltzmann model
$f_i(\mathbf{x},t)$	distribution function
$f_i^{eq}(\mathbf{x}, t)$	equilibrium distribution function
K_{ef}	effective permeability
$\mathbf{K}_{tow}$	permeability tensor
K_{tow}	tow permeability
L	length of computational domain
m	molecular weight
P	pressure
R	universal gas constant
$S_{\alpha,\beta}$	Einstein summation convention
T	absolute temperature
$\mathbf{u}$	velocity vector
u_x	velocity in x direction
u_y	velocity in y direction
$\mathbf{x}$	position vector

Greek letters

β	a parameter controlling the magnitude of the momentum sink
δt	time step
δx	the distance between abutting lattices
ε	effective porosity
ε_{min}	the ratio of void area to the area of cross section at the plane $x = 25$
ε_{nom}	nominal porosity
ε_{tow}	porosity of fiber tows
μ	viscosity of fluid
μ_e	effective viscosity
ν	kinematic viscosity
ρ	density of fluid
τ_ν	relaxation time
ω_i	weight coefficient for the lattice Boltzmann model

Subscripts

in	inlet
max	maximum value
min	minimum value
out	outlet
x	x direction
y	y direction
z	z direction

(PTFE) not to be congested with liquid water [2]. Water flow in GDL was experimentally investigated for various thicknesses and pore sizes in Benziger et al. [3]. Paganin et al. [2] observed a performance decrement at higher current densities when the GDL thickness is increased. The thickness of the GDL was optimized by a mathematical modeling in Inoue et al. [4] and by cell performance tests in Lee et al. [5] and Jordan et al. [6], with various GDL parameters such as porosity and thickness. A thin GDL with small porosity results in good electrical conductivity, however, efficient mass transport requires large pores. In a small and long serpentine flow channel, reactants can directly cross to neighboring channels due to high pressure gradient and short path [7–9]. It has been found that such cross flow plays an important role for an effective removal of liquid water from the gas diffusion layer [10]. The amount of cross flow is strongly correlated with the thickness and permeability of the GDL [7,8].

Present study presents the application of lattice Boltzmann (LB) method to the micro-scale flow simulation of reactant in the GDL of a PEM fuel cell. The LB method has been accepted as a new computational tool for a variety of fluid transport phenomena [11,12]. It was applied to incompressible fluid flows [13,14], transport of passive scalars [15], miscible and immiscible fluids in complex geometries [16] and two-phase flow with phase change [17]. The kinetic nature of the LB method was also shown to be applicable to simulation of chemical reaction in micro- and meso-scopic flow [18] and electrokinetic transport phenomena [19]. We used the porous LB model developed by Spaid and Phelan [20] to simulate the reactant flow in porous electrode made of carbon cloth, which is a heterogeneous porous medium. The model is equivalent to solving a Stokes/Brinkman formulation to allow fluid transport through finite sized porous objects by treating them as an effective medium with a known permeability. Due to the dynamic nature of the LB calculations, the method has advantage of being able to capture the flow dynamics leading up to the steady solution of the Stokes and Brinkman equations. The electrode is modeled as void space and circular (cylinder in 3-D) porous region which has a certain value of permeability. The effective permeability of the media from 2-D simulation is validated by comparing the LB result with a semi-analytical lubrication model described by Phelan and Wise [21]. The effect of fiber tow orientation on the effective permeability of the porous medium has been investigated using three-dimensional LB model within the wide ranges of tow permeability and porosity.

2. Numerical section

2.1. Governing equations

Modeling micro-scale flow in fibrous porous media differs from the fluid mechanics problems in homogenous porous media in that there exist void spaces between fiber tows, as well as porous regions comprised of the tow itself. A conventional treatment of flow problems in which there exists a combination of void and porous regions involves application of the Stokes and Brinkman equations. Fluid flow in the open regions is governed by the Stokes equation given by

$$\mu \nabla^2 \mathbf{u} = \nabla P \tag{1}$$

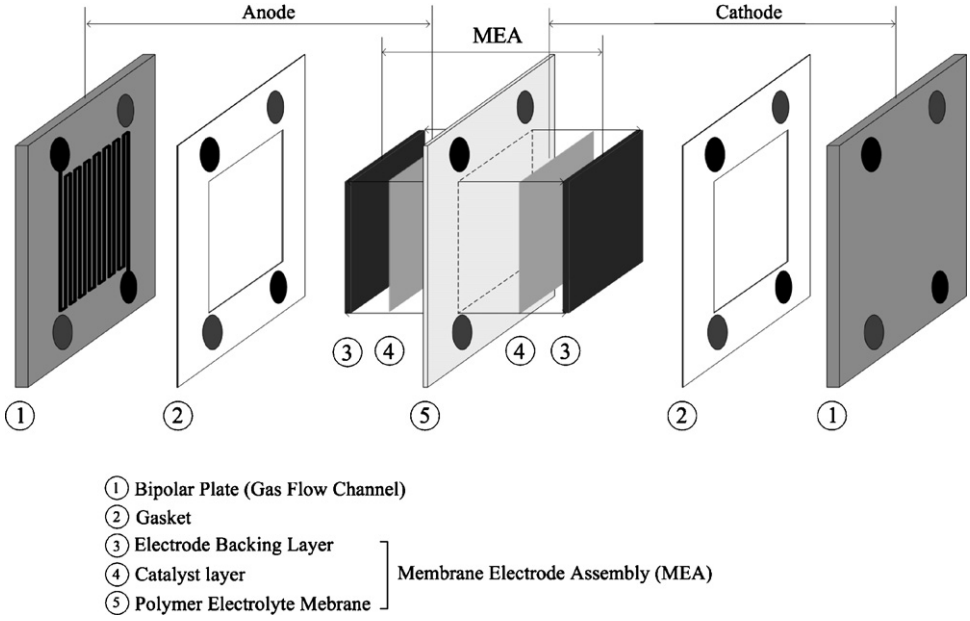

Fig. 1. Schematic of a polymer electrolyte fuel cell assembly.

where μ is viscosity, $\mathbf{u}$ is velocity vector and P is pressure. Inside the porous tows, the flow is modeled by the Brinkman equation,

$$\mu_e \nabla^2 \langle \mathbf{u} \rangle - \frac{\mu}{\mathbf{K}_{tow}} \cdot \langle \mathbf{u} \rangle = \nabla \langle P \rangle \tag{2}$$

where $\mathbf{K}_{tow}$ is the permeability tensor for the fiber bundles, and μ_e is the effective viscosity. The velocity and pressure are volume-averaged in the porous region. μ_e is assumed to be the same as μ since their relationship is not of primary importance for the present work. It is evident from Eq. (2) that the Brinkman equation reduces to Darcy's law far from the void spaces when velocity gradients are small. At the interface between the open and porous regions, the Stokes/Brinkman formulation satisfies the proper boundary conditions such as the continuity of velocity and stress [20]. Eqs. (2) and (3) are coupled with the continuity equation given by

$$\nabla \cdot \mathbf{u} = 0 \tag{3}$$

where the velocity in Eq. (3) must be replaced by the volume-averaged velocity $\langle \mathbf{u} \rangle$ within the fiber tows.

2.2. Lattice Boltzmann method

The LB method is based on a finite number of identical particles that go through collision and propagation successively on prefixed paths in space. The following single-component lattice Boltzmann equation describes evolution of the distribution function, $f_i(\mathbf{x},t)$, with the BGK collision term [22,23],

$$f_i(\mathbf{x} + \mathbf{e}_i \delta_t, t + \delta_t) - f_i(\mathbf{x}, t) = -\frac{f_i(\mathbf{x}, t) - f_i^{eq}(\mathbf{x}, t)}{\tau_v}, \tag{4}$$

where $\mathbf{e}_i$'s are the discrete velocities, δ_t the time step and τ_v is the relaxation time. f_i^{eq} represents the equilibrium distribution of f_i given as

$$f_i^{eq}(\rho, \mathbf{u}) = \omega_i \rho \left[1 + \frac{\mathbf{e}_i \cdot \mathbf{u}}{RT} + \frac{(\mathbf{e}_i \cdot \mathbf{u})^2}{2(RT)^2} - \frac{\mathbf{u} \cdot \mathbf{u}}{2RT} \right],$$

$$\omega_i = \begin{cases} 4/9 & i = 0 \\ 1/9 & i = 1, 2, 3, 4 \\ 1/36 & i = 5, 6, 7, 8 \end{cases} \tag{5}$$

where ω_i's are the associated weight coefficients, R the universal gas constant and T is the absolute temperature. In Fig. 2(a), the velocity vectors, $\mathbf{e}_i$, for the two-dimensional 9-speed model (D2Q9) are shown to be

$$\mathbf{e}_i = \begin{bmatrix} (0,0), & \text{for } i = 0 \\ c\left(\cos\dfrac{i-1}{2}\pi,\ \sin\dfrac{i-1}{2}\pi\right), & \text{for } i = 1, 2, 3, 4 \\ \sqrt{2}c\left(\cos\dfrac{i-4-1/2}{2}\pi,\ \sin\dfrac{i-4-1/2}{2}\pi\right), & \text{for } i = 5, 6, 7, 8 \end{bmatrix}, \tag{6}$$

where $c = \delta_x/\delta_t$, and δ_x is the distance between lattice points. The speed of the sound is $c/\sqrt{3}$ in the phase space and accordingly we have $RT = c^2/3$. The macroscopic number density, $\rho(\mathbf{x},t)$, and the velocity, $\mathbf{u}(\mathbf{x},t)$, of the fluid are obtained as

$$\rho = \sum_{i=0}^{8} m f_i, \tag{7}$$

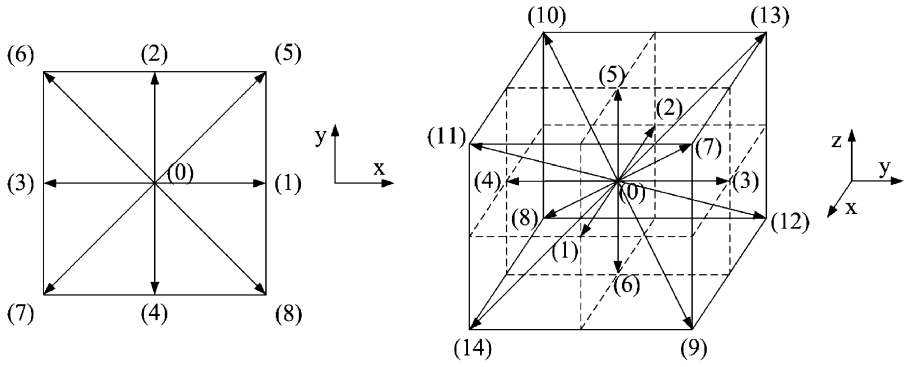

Fig. 2. (a) A microscopic picture of the woven carbon cloth gas diffusion media (white square represents the computational domain and white dotted circle represents the region of tow), (b) a schematic of 2-D numerical model for porous medium.

$$\rho\mathbf{u} = \sum_{i=0}^{8} m f_i \mathbf{e}_i, \tag{8}$$

where the molecular weight, m, is assumed to be unity in the present work. The kinematic viscosity is related to the relaxation time as

$$\nu = \frac{(2\tau_\nu - 1)}{6}\frac{\delta_x^2}{\delta_t}. \tag{9}$$

In this work, δ_x and δ_t are set to be unity for convenience, and thus, the fluid pressure is given in terms of the fluid density as $p = \rho/3$.

The 3-D LBM is also based on LBGK model and solves Eq. (4) in a three-dimensional space. We use a three-dimensional 15-speed model (D3Q15) for the present work [25,26] in which the velocity vectors, $\mathbf{e}_i$, $i = 0, 1, \ldots, 14$, are the column vectors of the following matrix:

$$E = \begin{bmatrix} 0 & 1 & -1 & 0 & 0 & 0 & 0 & 1 & -1 & 1 & -1 & 1 & -1 & 1 & -1 \\ 0 & 0 & 0 & 1 & -1 & 0 & 0 & 1 & -1 & 1 & -1 & -1 & 1 & -1 & 1 \\ 0 & 0 & 0 & 0 & 0 & 1 & -1 & 1 & -1 & -1 & 1 & 1 & -1 & -1 & 1 \end{bmatrix} \tag{10}$$

The density per node, ρ, and the macroscopic flow velocity, $\mathbf{u} = (u_x, u_y, u_z)$, are defined in terms of the particle distribution function by

$$\sum_{i=0}^{14} f_i = \rho \tag{11}$$

$$\sum_{i=0}^{14} f_i \mathbf{e}_i = \rho\mathbf{u} \tag{12}$$

The equilibrium can be chosen as [26]

$$f_0^{(\mathrm{eq})} = \frac{1}{8}\rho - \frac{1}{3}\rho\mathbf{u}\cdot\mathbf{u}, \tag{13}$$

$$f_i^{(\mathrm{eq})} = \frac{1}{8}\rho + \frac{1}{3}\rho\mathbf{e}_i\cdot\mathbf{u} + \frac{1}{2}\rho(\mathbf{e}_i\cdot\mathbf{u})^2 - \frac{1}{6}\rho\mathbf{u}\cdot\mathbf{u},$$
$$i = 1, \ldots, 6: \quad \text{Class I} \tag{14}$$

$$f_i^{(\mathrm{eq})} = \frac{1}{64}\rho + \frac{1}{24}\rho\mathbf{e}_i\cdot\mathbf{u} + \frac{1}{16}\rho(\mathbf{e}_i\cdot\mathbf{u})^2 - \frac{1}{48}\rho\mathbf{u}\cdot\mathbf{u},$$
$$i = 7, \ldots, 14: \quad \text{Class II} \tag{15}$$

where Classes I and II indicate the lattices at the face and at the corner of 3-D computational lattice structure, respectively, as shown in Fig. 2(b). Through Chapman-Enskog expansion, the Eqs. (4) and (5) lead to the Navier–Stokes equations near the incompressible limit [24]. They are given by continuity equation,

$$\frac{\partial\rho}{\partial t} + \nabla\cdot(\rho\mathbf{u}) = 0, \tag{16}$$

and the momentum equation,

$$\partial_t(\rho u_\alpha) + \partial_\beta(\rho u_\alpha u_\beta) = -\partial_\alpha(c_s^2\rho) + \partial_\beta(2\nu\rho S_{\alpha\beta}), \tag{17}$$

where the Einstein summation convention is used. $S_{\alpha\beta} = (\partial_\alpha u_\beta + \partial_\beta u_\alpha)/2$ is the strain-rate tensor. The sound speed is $c_s = \sqrt{3/8}$ for the 3-D LB model.

2.3. Lattice Boltzmann model for a porous medium

To recover the Brinkman equation using a lattice Boltzmann method, it is necessary to modify the standard equilibrium distribution function to reduce the magnitude of the momentum, leaving the direction of momentum unchanged. This may be achieved by altering the velocity $\mathbf{u}(\mathbf{x},t)$ in the equilibrium distribution function by incorporating a forcing term given by

$$\mathbf{U} = \mathbf{u}(\mathbf{x}, t) + s(\mathbf{x})\frac{\tau\mathbf{F}(\mathbf{x}, t)}{\rho(\mathbf{x}, t)}, \tag{18}$$

where $\mathbf{U}$ replaces $\mathbf{u}$ in Eq. (5) for the equilibrium distribution function, and the variable $s(\mathbf{x},t)$ is either 0 or 1 depending on

weather a lattice site is located in a void or porous region, respectively. Eq. (18) has also been used to incorporate a body force such as fluid–solid interaction potential [27], fluid–fluid interaction potential [28] and electrostatic potential between electronically charged ions [19]. The form of the forcing term $\mathbf{F}(\mathbf{x},t)$ which is needed to recover the Brinkman equation is given by

$$\mathbf{F}(\mathbf{x}, t) = -\beta\rho(\mathbf{x}, t)\mathbf{u}(x, t), \tag{19}$$

where β is a parameter controlling the magnitude of the momentum sink. From Eqs. (10) and (11), the equilibrium velocity in a Brinkman site ($s(\mathbf{x},t) = 1.0$) is defined as

$$\mathbf{U} = \mathbf{u}(\mathbf{x}, t)(1 - \beta\tau). \tag{20}$$

In Spaid and Phelan [20], a proof is given that the above formulation removes a specific amount of momentum in the collision process, and hence recovers the Brinkman equation. Then, the LB equation in a Brinkman site is given for the steady state as

$$v\nabla^2\mathbf{u} - \beta\mathbf{u} = \frac{1}{\rho}\nabla P. \tag{21}$$

Eq. (21) reproduces the Brinkman equation if $\beta = \nu/\mathbf{K}_{\text{tow}}$ in which both the kinematic viscosity and the tow permeability are expressed in lattice units [21].

2.4. Boundary conditions

The practical flow situation in a PEM fuel cell employs some forms of flow regulations at the inlet, outlet and other boundaries. Common types of regulations are constant-velocity, constant pressure and no-slip wall. For the D2Q9 model, we utilized the bounce-back rule to determine unknown part of particle distribution functions [25]. As an example, it is considered that the boundary is aligned with the x-direction with f_4, f_7, f_8 pointing into the wall as shown in Fig. 2(a). After streaming, $f_0, f_1, f_3, f_4, f_7, f_8$ are known. Supposing that u_x and u_y are specified on the boundary Eq. (7) and (8) are used to determine f_2, f_5, f_6 and ρ as follows:

$$f_2 + f_5 + f_6 = \rho - (f_0 + f_1 + f_3 + f_4 + f_7 + f_8), \tag{22}$$

$$f_5 - f_6 = \rho u_x - (f_1 - f_3 - f_7 + f_8), \tag{23}$$

$$f_2 + f_5 + f_6 = \rho u_y + (f_4 + f_7 + f_8), \tag{24}$$

$$\rho = \frac{1}{1 - u_y}[f_0 + f_1 + f_3 + 2(f_4 + f_7 + f_8)] \tag{25}$$

To close the system of equations above, we assume the bounce back rule for the non-equilibrium part of the particle distribution normal to the boundary (in this case, $f_2 - f_2^{(\text{eq})} = f_4 - f_4^{(\text{eq})}$). With f_2 known f_5 and f_6 can be found, thus,

$$f_2 = f_4 + \frac{2}{3}\rho u_y \tag{26}$$

$$f_5 = f_7 - \frac{1}{2}(f_1 - f_3) + \frac{1}{2}\rho u_x + \frac{1}{6}\rho u_y \tag{27}$$

$$f_6 = f_8 - \frac{1}{2}(f_1 - f_3) - \frac{1}{2}\rho u_x + \frac{1}{6}\rho u_y \tag{28}$$

The collision is also applied to the boundary nodes. No slip wall can be achieved applying velocities on the wall equals zero ($u_x = u_y = 0$) on the boundary. Similarly, when the density (pressure) is known on the boundary and the velocity is assumed to be normal to the boundary ($u_x = 0$), the unknowns (u_y, f_5, f_6) can be determined from Eqs. (22)–(25) as:

$$u_y = 1 - \frac{[f_0 + f_1 + f_3 + 2(f_4 + f_7 + f_8)]}{\rho_{\text{in}}} \tag{29}$$

$$f_2 = f_4 + \frac{2}{3}\rho u_y \tag{30}$$

$$f_5 = f_7 - \frac{1}{2}(f_1 - f_3) + \frac{1}{6}\rho u_y \tag{31}$$

$$f_6 = f_8 - \frac{1}{2}(f_1 - f_3) + \frac{1}{6}\rho u_y \tag{32}$$

We followed Maier et al. [26] to impose boundary conditions for the 3-D LB simulations. To apply the constant pressure, the incoming populations through boundary are determined using the first-order extrapolation rule as:

$$f_i(\mathbf{x}, t) - f_i(\mathbf{x} + \mathbf{e}_i, t) = -[f_j(\mathbf{x}, t) - f_j(\mathbf{x} + \mathbf{e}_j, t)] \tag{33}$$

where $\mathbf{e}_j$ is the outward vectors, which is the mirror image of $\mathbf{e}_i$ at the boundary. This extrapolated populations are used to calculate a provisional density, ρ, from Eq. (11). The mass addition is used next to achieve the prescribed density, ρ_{in}, at the boundary. The mass is added to the incoming Class II links are obtained as:

$$f_i(\mathbf{x}, t) = f_j(\mathbf{x}, t) - \frac{1}{4}\bar{\rho} \tag{34}$$

where $\bar{\rho} = \rho - \rho_{\text{in}}$. The set of incoming class II links satisfies the relation, $\mathbf{e}_i \cdot \mathbf{e}_k = 1$, for indices $i \in$ class II. The no slip boundary condition can be enforced by using the bounce-back operation to set provisional values for the unknown populations, and then by redistributing these populations to achieve a prescribed tangential velocity at the wall. The bounce-back operation defines the density at the wall, and the mass redistribution defines the tangential momentum. The entire operation is executed after streaming and before collision. More details can be found in Maier et al. [26].

3. Results and discussion

The enhancement of the reactant transportation in the GDL has been an important issue to improve the performance of a PEM fuel cell especially at high current density. The flow distribution in the GDL is also strongly affected by the cross flow that is also known to be effective on the liquid water removal from the GDL [7–10]. Therefore, the characteristic of reactant flow in the GDL would be one of the most important factors for the design and optimization of a PEM fuel cell. The GDL has been conventionally modeled as a homogeneous porous medium, as pointed out previously, however, the homogeneous model is not proper

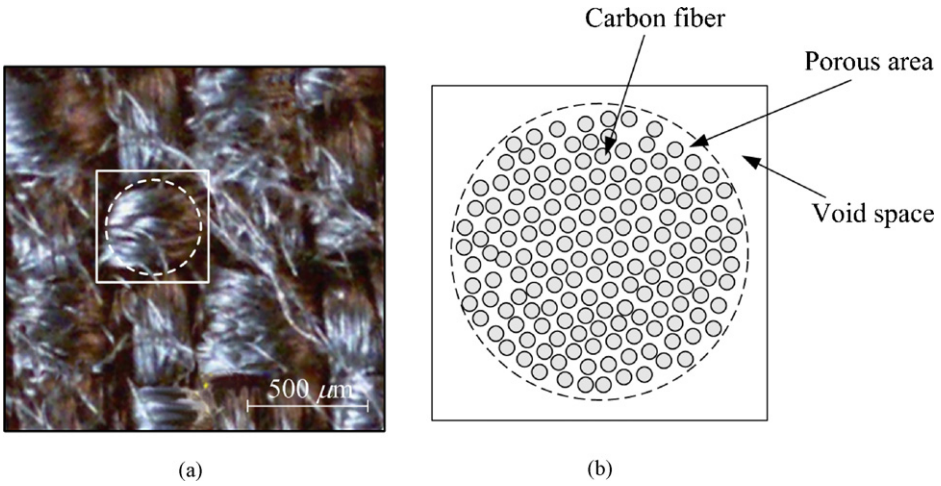

Fig. 3. Lattice structures of the 2-D and 3-D lattice Boltzmann model: (a) D2Q9 and (b) D3Q15.

for the investigation of the flow characteristics in a heterogeneous porous medium such as the GDL made of woven carbon cloth in a PEM fuel cell. The permeability of GDL depends on its fiber tow orientation and its non-isotropic permeability is critical on the flow and concentration distribution in a PEM fuel cell. For further detailed investigations, the LB method is applied to the flow simulation in the GDL of a PEM fuel cell to verify the effect of fiber tow orientation on the effective permeability of the porous medium.

3.1. Two dimensional LB simulations

In this section, the two dimensional LB model for the heterogeneous porous medium is validated by comparing the LB simulation results with the lubrication model [21]. The GDL is modeled as consisting of void space and fiber tow area which has certain permeability. Eqs. (4)–(9) and (18)–(20) are solved for a transverse flow over 2-D porous circle as shown in Fig. 3(b). For a general shape of an elliptical porous tow, the effective porosity of the medium is given by the lubrication model as:

$$\varepsilon = 1 - \frac{\pi}{4}\frac{ab}{L_x L_y}(1 - \varepsilon_{\text{tow}}) \tag{35}$$

where a, b, L_x and L_y are defined in Fig. 4, and ε_{tow} is the porosity of the fiber tow. It is often useful to refer to a nominal porosity, which is based on the tow shape alone, defined as

$$\varepsilon_{\text{nom}} = 1 - \frac{\pi}{4}\frac{ab}{L_x L_y}. \tag{36}$$

Flow is driven in the y direction by a pressure difference between the boundaries $y = -L_y$ and $y = L_y$, while periodic boundary conditions are imposed at $x = -L_x$ and $x = L_x$. Then, regardless of the amount of the applied pressure, the effective permeability for the test geometry can be found as [21]

$$K_{\text{ef}} \approx \frac{2L_y/L_x}{\int_{-L_y}^{L_y} 1/f \, \mathrm{d}y} \tag{37}$$

where

$$f = \frac{h^3}{3} + K_{\text{tow}}[\varepsilon_{\text{tow}} g + (1 + \varepsilon_{\text{tow}})h + K_{\text{tow}}^{-1/2} h^2 \coth(K_{\text{tow}}^{-1/2} g)] \tag{38}$$

Here, g and h are defined in Fig. 4.

The porous tow is modeled as a circle ($a = b = d/2$) in a square computational domain ($L_x = L_y = L/2$) for the present 2-D simulation. Fifty-one and 44 grid points are assigned for the length (L) of computational domain and the diameter (d) of the porous circle, respectively. Simulations are conducted with the constant value of $\beta = 0.125$ while the value of tow permeability, K_{tow}, is changed within the range of 0.1–0.0001. The same boundary conditions described for the lubrication model are applied; constant pressure at $y = -L_y$ (inlet) and $y = L_y$ (outlet) and periodic condition at $x = -L_x$ and $x = L_x$.

Fig. 5(a) presents the velocity and pressure distributions in the porous medium when the tow permeability, K_{tow}, is 0.01. The velocity vectors are normalized by the maximum velocity

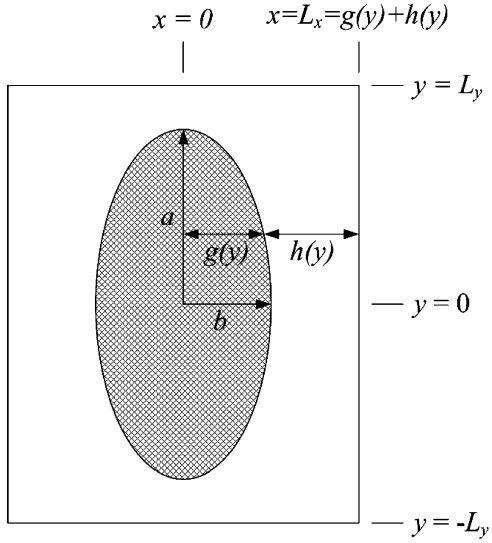

Fig. 4. Geometry for transverse flow in the y direction over porous tows with elliptical cross section, indicating parameters used in the lubrication model [21].

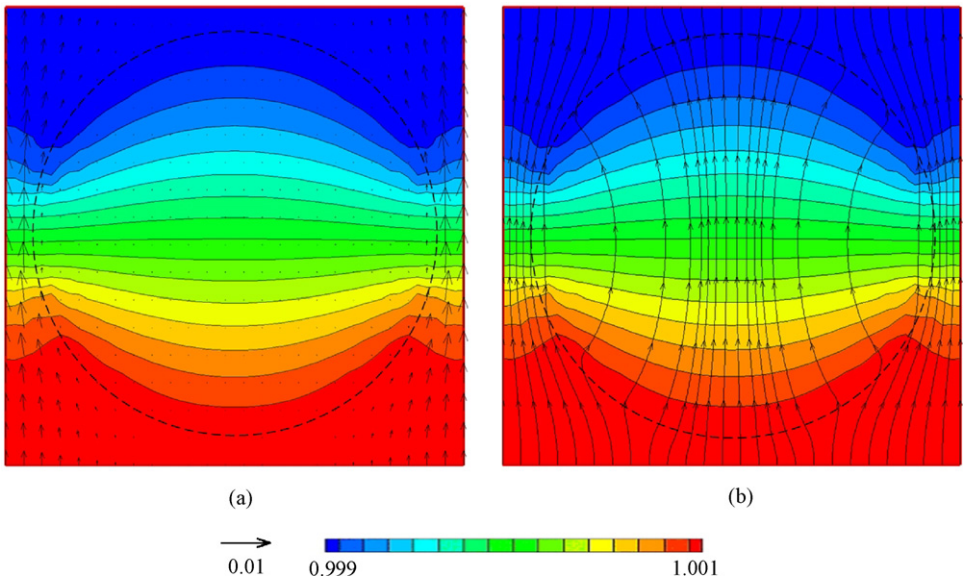

Fig. 5. 2-D lattice Boltzmann simulation results: (a) pressure contour with velocity vectors and (b) pressure contour with streamlines; $K_{tow} = 0.01$.

in the computational domain where the tow area is marked as a dashed circle. It is seen that the magnitude of velocity is substantially smaller inside the tow area than outside the tow area due to the flow resistance caused by the low permeability of the tow area. The pressure contours are symmetrical profiles for the upstream and downstream divided by a straight contour that is normal to the mean flow direction (y-direction). The magnitude of velocity is the largest at the middle of periodic boundaries ($x = -L_x$, $x = L_x$) where the pressure gradient is also the largest. Fig. 5(b) shows the streamlines with the pressure contours in the porous medium. Although the magnitude of velocity in the porous medium is very small the flow permeates into the porous tow area and the resultant streamlines are normal to the pressure contour. As the value of tow permeability increases the tow behaves like a solid obstacle, and thus, the flow permeation becomes negligible inside the tow area.

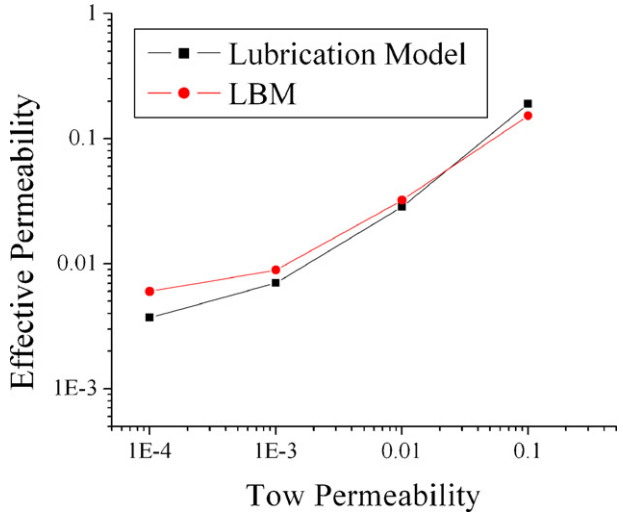

Fig. 6. Comparison of the effective permeability between the LB simulation (circles) and the lubrication model (square) [21], as a function of the dimensionless tow permeability; the nominal porosity (ε_{nom}) of porous medium is 0.4.

In Fig. 6, the resultant effective permeabilities of the porous medium are compared between the LB simulation and the lubrication model to prove the validity of the present LB model. The effective permeability is calculated using Darcy's law for the LB simulation,

$$\langle \mathbf{u} \rangle = -\frac{K_{tow} \cdot \nabla \langle P \rangle}{\mu} \tag{39}$$

where $\langle \mathbf{u} \rangle$ is the average velocity in the computational domain. The LB simulation shows a fair agreement with the lubrication model although the deviation becomes noticeable at small permeability, 10^{-4}. It seems that the hexagonal LB model in Spaid and Phelan [20] shows a better agreement with the results of lubrication model. This may be attributed to the fact that the hexagonal grid (D2Q7) fits better for the circular porous tow than the rectangular grid (D2Q9) does in the present simulation. The LB simulation involves considerable numerical errors for the value of tow permeability smaller than 10^{-4}. This is attributed to that the relaxation time, τ, is also decreased along with the value of tow permeability as shown in Table 1.

3.2. Three-dimensional LB simulations; effective permeability versus tow orientations

The architecture of the fiber preform is one of the most important factors which determine the anisotropy of textile porous medium. Much effort has been made to measure the perme-

Table 1
Values of the relaxation time τ_v for various tow permeability K_{tow}

K_{tow}	τ_v
0.1	1.325
0.01	0.5825
0.001	0.50825
0.0001	0.500825

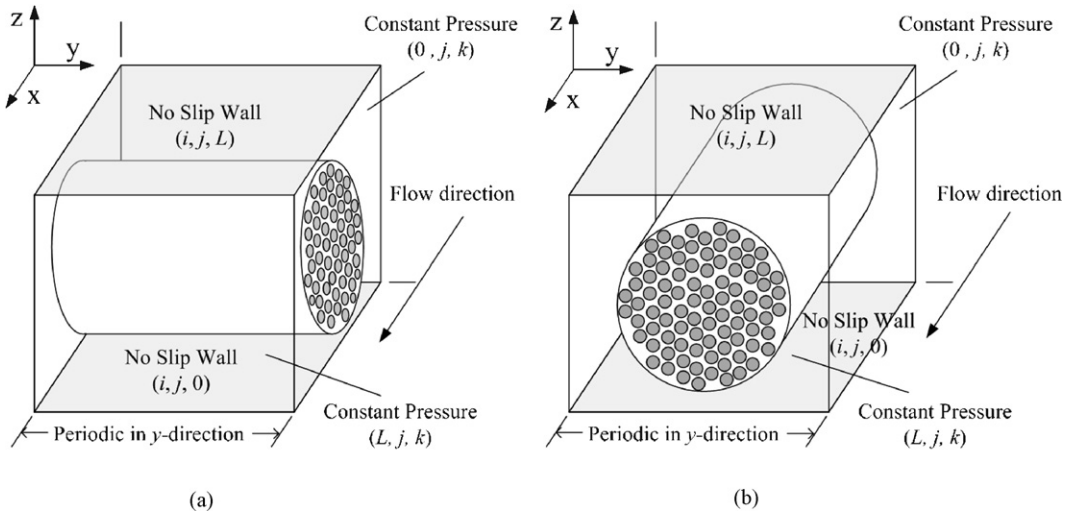

Fig. 7. Schematic of 3-D model for the two different tow directions: (a) Case A—flow across the tow direction and (b) Case B—flow along the tow direction.

ability of various materials for a wide range of flow conditions [29–34] and such experimental measurements were correlated with the types of fiber preforms in Jackson and James [35]. Textile porous medium such as woven cloth can be modeled by capturing features of reciprocating patterns in the fiber preforms. The effect of different architecture and resulting fiber orientation on effective permeability of porous medium was studied analytically by Yu and Lee [36] in which a simplified permeability model was developed from one-dimensional Stokes/Brinkman equation based on the proposed rectangular unit cell geometry.

In this work, the porous LB model is applied to the 3-D simulation of the flow in fibrous porous medium to investigate the effect of the tow orientation on the effective permeability. As shown in Fig. 7, the fiber tow is modeled as a circular cylinder which has certain permeability in a cubical computational domain consisted of $51 \times 51 \times 51$ lattice points. The tow has a constant length of $0.92L$ (equivalent to 47 lattice points) and various diameters 0.5–$0.9L$ (equivalent to 25–45 lattice points). The point of origin is set at the corner of the cubical computational domain as shown in Fig. 7. No-slip wall is assigned as the boundary conditions for the top and bottom surfaces ($z = 0$ and $z = L$) and periodic condition for the right and left walls ($y = 0$ and $y = L$). Constant pressure is applied at the plane $x = 0$ and $x = L$ to drive the mean flow motion in the x-direction. Two different flow configurations are considered in this study; Fig. 7(a) represents the case when the fiber tow is normal to the mean flow direction (x-direction) while Fig. 7(b) when the fiber tow is parallel with the mean flow direction. Hereinafter, the flow configurations in Fig. 7(a) and (b) are referred to as Case A and Case B, respectively.

Fig. 8 shows the streamlines and the contour plots for the magnitude of the x-component velocity (U_x) at the two different planes ($x = 25$ and $y = 25$) to present the flow structures. The magnitude of velocity is normalized using the maximum velocity in the computational domain. On the plane $x = 25$ in Fig. 8(a), it is seen that the magnitude of velocity is the largest between the wall and tow boundary and negligible inside the tow region. The void area changes along the mean flow direction for Case A since the fiber tow is normal to the mean flow direction. Case A has symmetrical velocity profiles on the plane $y = 25$ indicating that the flow is accelerated and decelerated before and after the plane $x = 25$ with the noticeable flow permeation into the porous region. On the other hand, the magnitude of x-component velocity is consistent for Case B due to the fixed void area along the mean flow direction. The flow permeation into the porous region is almost negligible in Case B.

In Fig. 9, the effective permeability of the porous medium is obtained by the LB simulation and presented as a function of tow permeability for various tow diameters, $0.5L$–$0.9L$. The effective permeability increases as the tow permeability increases for both the Case A and B. It is larger for the smaller tow diameter with the larger rate of increment against the increasing tow permeability. Although Case A and B present similar trends against the increasing tow diameter and permeability Case B has substantially larger effective permeability. This is mainly caused by that Case B has a much smaller minimal void area than Case A as shown in Table 2. For instance, the nominal porosity on the plane $x = 25$ for Case A and B in Fig. 7 are 0.74 and 0.5, respectively. Furthermore, it seems that the effect of the drag by the no-slip wall is more significant in Case A. The combinational effects of the smaller void area and larger wall drag result in substantially lower effective permeability for Case A. Similar phenomenon was reported by an analytical analysis in Yu and Lee [36] and by experimental measurements in Jackson and James [35]. The effect of this phenomenon could be significant on the flow and

Table 2
Nominal porosity of 3-D porous medium (ε_{nom}, the ratio of the void space to total volume) and the ratio of the void area to the area of cross-section at the plane $x = 25$ (ε_{min})

d_{tow}	ε_{nom}	ε_{min} (Case A)	ε_{min} (Case B)
$0.5L$	0.82	0.54	0.80
$0.6L$	0.74	0.45	0.72
$0.7L$	0.65	0.35	0.62
$0.8L$	0.54	0.26	0.50
$0.9L$	0.41	0.17	0.36

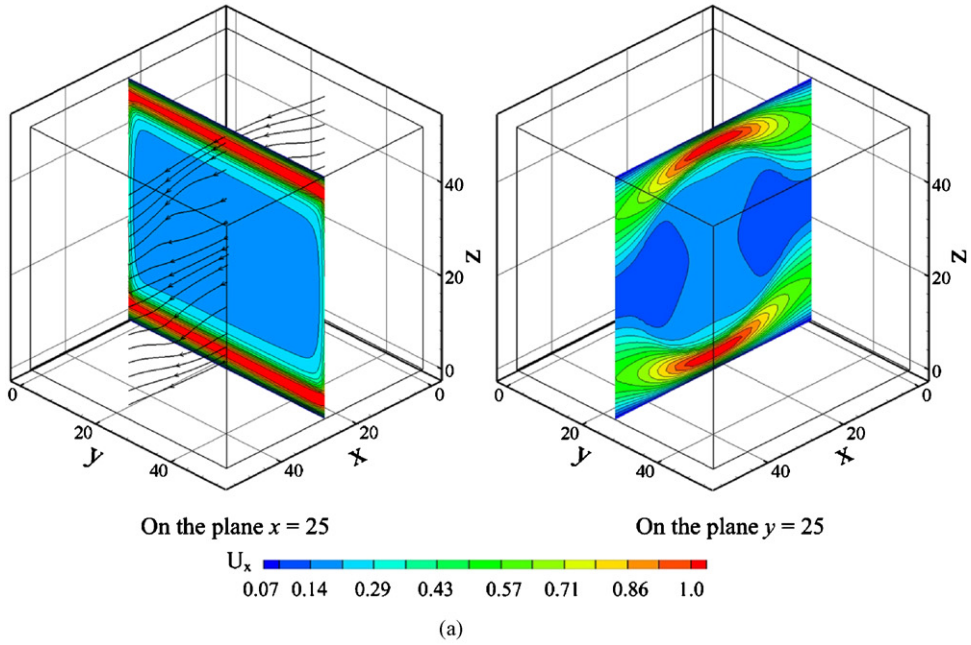

Fig. 8. Contour plots for the x-component velocity (U_x) with streamlines at two cross-sectional planes; $d_{tow} = 0.8L$, $K_{tow} = 0.05$: (a) Case A and (b) Case B; the magnitude of velocity is normalized using maximum velocity in the domain.

concentration distributions in the GDL of a PEM fuel cell since the cross flow can be enhanced or reduced depending on the local tow orientation. The liquid water accumulation may be increased when Case A is close to the U-turn of flow channel where the velocity of cross flow is much lower than other areas [7,10].

Fig. 10 compares the effective permeability of the porous medium between Case A and B as a function of tow diameter when the tow permeability is 0.1 and 0.01. The effective permeability decreases as the tow diameter increases for the same value of tow permeability. Both the effect of fiber orientation and tow permeability are more significant when the diameter of the tow is smaller. The effect of tow direction is dominant over the effective permeability when the tow diameter is small while the effect of permeability becomes more significant as the tow diameter decreases.

Fig. 11 shows the effective permeability of the porous medium as a function of nominal porosity when the permeability, K_{tow}, is 0.1 and 0.01. According to Eq. (35), the nominal porosity of the porous medium decreases as the tow permeability increases and the resultant difference between $K_{tow} = 0.1$ and 0.01 is about 9%. The effective permeability is distinct for different tow permeability (0.1 and 0.01) shown in Fig. 10 while the data with different tow permeability seems to collapse onto

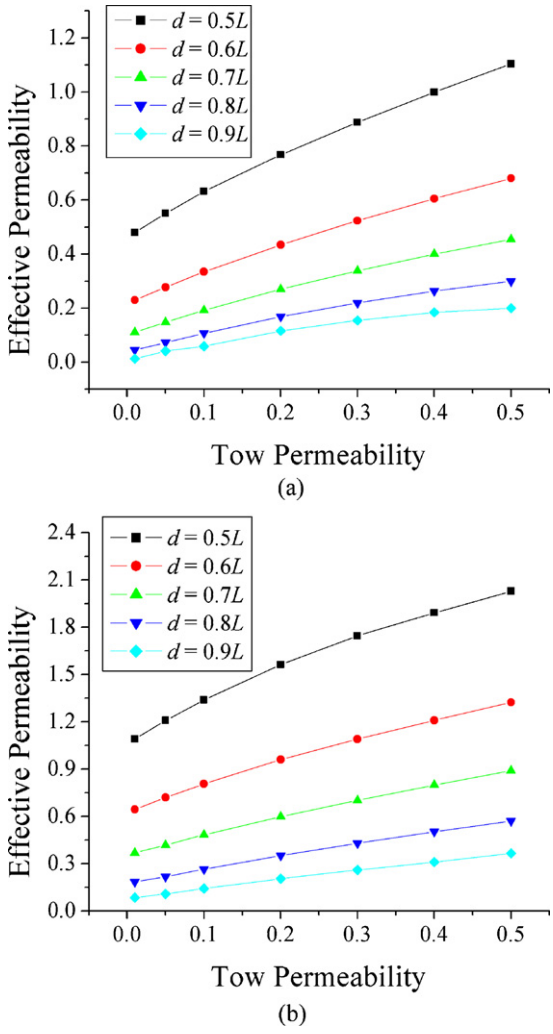

Fig. 9. Effective permeability of the porous medium as a function of tow permeability for various tow diameters: (a) Case A and (b) Case B.

a single line when plotted as a function of the nominal porosity, but the lines are different for the two fiber orientations of parallel or normal to the flow direction, as clearly shown in Fig. 11. This might suggest that the actual effective permeability for the

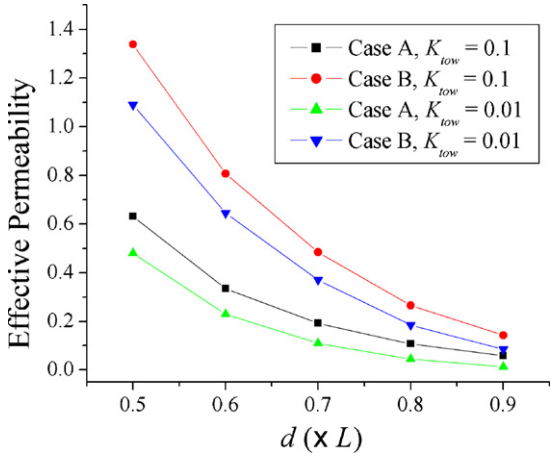

Fig. 10. Comparison of the effective permeability of the porous medium as a function of tow diameter.

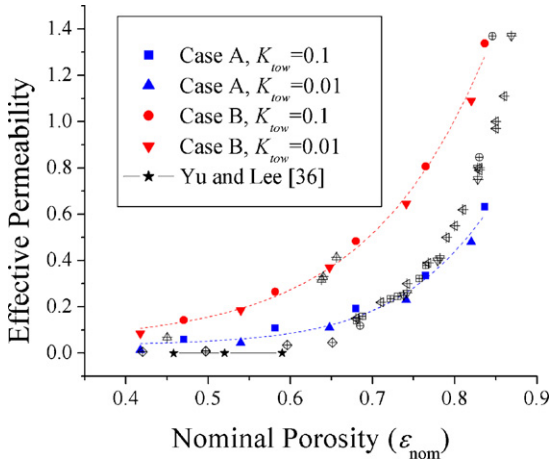

Fig. 11. Comparison of the effective permeability of the porous medium with experimental measurements available in literature; (■) Carman [29], (⊕) Wiggins et al. [30], (⧋) Sullivan [31], (⧩) Brown [32], (⧓) Bergelin et al. [33], (⧁) Ingmanson et al. [34]; all these experimental measurements are also cited and available in Jackson and James [35].

fibrous materials will be bounded by these two lines if the fiber is inclined to the flow direction. As seen in Fig. 11, most of the experimental data points [29–33] are indeed falling between these two lines.

3.3. Numerical stability

The LB method provides a valid alternative to solving the Stokes and Brinkman equations for elliptical equations. Since the LB method is inherently dynamic with the Stokes and Brinkman equations it would be a reasonable choice if the particular application requires the unsteady flow dynamics. However, if only the steady results are desired, standard methods such as finite difference or finite element calculations could be more efficient. It has been found that the present method is numerically unstable for parameter values v and K_{tow} such that $\beta = v/K_{\text{tow}} > 2$ as also indicated in Spaid and Phelan [20]. The origin of the numerical instability is the depletion of distributions components, which point in the direction of the velocity, ultimately leading to negative values for these distributions and numerical instability. Therefore, the case of an infinite momentum sink equivalent to an object with zero permeability must be treated with other type of technique such as wall boundary conditions.

The results of the present 2-D simulation covers the range of non-dimensional effective permeability from 10^{-4} to 1, which is equivalent to 10^{-12} to 10^{-8} m^2 in a physical domain if the characteristic length scale is assumed as 100 μm. This fairly covers the range for the permeability of the actual GDL in a PEM fuel cell in many literatures [7–10]. However, the present 3-D simulation does not cover this range with the current number of lattice points. The modeling flow through heterogeneous material having very low permeability requires larger lattices due to the stability constraints on β. For the case of heterogeneous porous media, additional stability issues may arise when considering flow through a near impermeable object at a low

nominal porosity. In this case, the magnitude of the velocity may be quite large in the void fluid regions, and could cause numerical instability. Careful attention must be paid to the magnitude of the driving force in order to keep the velocity within the proper bounds.

4. Concluding remarks

In this study, the porous LB model for the Stokes/Brinkman formulation has been applied to the flow simulation in a heterogeneous porous medium such as the GDL made of woven carbon cloth in a PEM fuel cell. The GDL is modeled as a void space and fiber tow region, which has certain permeability. The LB model was validated by comparing the LB simulation results with an analytical calculation showing a good agreement for a wide range of tow permeability. The effective permeability of the porous medium is compared with analytical and experimental results in literature and the large variance of the effective permeability for the same porosity is explained in terms of the effect of tow permeability. The 3-D LB model is applied to investigate the effect of fiber tow orientation on the resultant effective permeability of a porous medium in a wide range of tow diameter and permeability. For the cases investigated, the effective permeability is substantially larger, as much as doubled, for the fiber orientation parallel with the mean flow direction, when compared to the case of the fibers normal to the mean flow direction.

One of the primary advantages of LB method for simulating fluid flows as compared to traditional numerical methods is their ability to robustly model interfaces between two or more fluids. The mechanism of liquid water accumulation in the GDL is of great interest for PEM fuel cell researchers since the phenomenon is one of the main mechanisms, which limit the performance of a PEM fuel cell. Conventional homogeneous porous model is not proper for the investigation of the liquid water accumulation in a heterogeneous porous medium due to the fact that the liquid water behavior inside the fiber tow is completely different from that in the void space. The binary fluid model with the present Stokes/Brinkman formulation implemented would provide a useful tool to investigate the mechanism of liquid water accumulation in the GDL of a PEM fuel cell.

Acknowledgment

This work was supported by AUTO21, the Network of Centers of Excellence, Canada.

References

[1] X. Li, Principles of Fuel Cells, Taylor & Francis, New York, 2006.
[2] V.A. Paganin, E.A. Ticcianelli, E.R. Gonzalez, J. Appl. Electrochem. 26 (3) (1996) 297.
[3] J. Benziger, J. Nehlsen, D. Blackwell, T. Brennan, J. Itescu, J. Membr. Sci. 261 (2005) 98–106.
[4] G. Inoue, Y. Matsukuma, M. Minemoto, J. Power Sources 154 (2006) 8–17.
[5] H. Lee, J. Park, D. Kim, T. Lee, J. Power Sources 131 (2004) 200–206.
[6] L. Jordan, A. Shukla, T. Beehrsing, N. Avery, B. Muddle, M. Forsyth, J. Power Sources (2000) 250–254.
[7] J. Park, X. Li, J. Power Sources 163 (2007) 853–863.
[8] G. Inoue, Y. Matsukuma, M. Minemoto, J. Power Sources 157 (2006) 136–152.
[9] T. Kanezaki, X. Li, J.J. Baschuk, J. Power Sources 162 (2006) 415–425.
[10] J. Park, X. Li, D. Tran, T. Abdel-Baset, D.S. Hussey, D.L. Jacobson, M. Arif, Neutron imaging investigation of liquid water distribution in and the performance of a PEM fuel cell, Int. J. Hydrogen Energy, in press.
[11] Y.H. Qian, D. D'Humieres, P. Lallenmand, Europhys. Lett. 17 (1992) 479.
[12] X. He, L. Luo, J. Stat. Phys. 88 (1997) 927.
[13] A. Cali, S. Succi, A. Cancelliere, R. Benzi, M. Gramignani, Phys. Rev. A 45 (1992) 5771.
[14] X.W. Shan, H.D. Chen, Phys. Rev. E 47 (1993) 1815.
[15] B.J. Palmer, D.R. Rector, Phys. Rev. E 61 (2000) 5295.
[16] S.P. Dawson, S. Chen, G.D. Doolen, J. Chem. Phys. 98 (1993) 1514.
[17] X. He, N. Li, Comput. Phys. Commun. 129 (2000) 158.
[18] B. Li, D.Y. Kwok, Int. J. Heat Mass Trans. 46 (2003) 4235.
[19] J. Park, K.Y. Huh, X. Li, J. Electroanal. Chem. 591 (2006) 141–148.
[20] M. Spaid, F.R. Phelan Jr., Phys. Fluids 9 (1997) 2468–2474.
[21] F.R. Phelan Jr., G. Wise, Composites 27A (1995) 25.
[22] P.L. Bhatnagar, E.P. Gross, M. Krook, Phys. Rev. 94 (1954) 511.
[23] X. He, L. Luo, Phys. Rev. E 56 (1997) 6811.
[24] H. Chen, S. Chen, W.H. Matthaeus, Phys. Rev. A 45 (1992) R5339.
[25] Q. Zou, X. He, Phys. Fluids 9 (1997) 1591–1598.
[26] R.S. Maier, R.S. Bernard, D.W. Grunau, Phys. Fluids 8 (1996) 1788–1801.
[27] N.S. Martys, H. Chen, Phys. Rev. E 53 (1996) 743.
[28] X. Shan, H. Chen, Phys. Rev. E 47 (1991) 4320.
[29] P.C. Carman, Soc. Chem. Industry (Trans. Commun.) 57 (1938) 225–234.
[30] E.J. Wiggins, W.B. Campbell, O. Maass, Can. J. Res. 17B (1939) 318–324.
[31] R.R. Sullivan, J. Appl. Phys. 13 (1942) 725–730.
[32] J.C. Brown, TAPPI 33 (1950) 130–137.
[33] O.P. Bergelin, G.A. Brown, H.L. Hull, F.W. Sullivan, Trans. ASME, August (1950) 881–888.
[34] W.L. Ingmanson, B.D. Andrews, R.C. Johnson, TAPPI 42 (1959) 840–849.
[35] G.W. Jackson, D.F. James, Can. J. Chem. Eng. 64 (1986) 364–374.
[36] B. Yu, L.J. Lee, Polym. Comp. 21 (2000) 660–685.